Numerical Heat Transfer, Part B, 60: 179–202, 2011

ISSN: 1040-7790 print/1521-0626 online
DOI: 10.1080/10407790.2011.601147

Taylor & Francis
Taylor & Francis Group

DEVELOPMENT OF AN UPWINDING SCHEME THROUGH THE MINIMIZATION OF MODIFIED WAVENUMBER ERROR FOR THE INCOMPRESSIBLE NAVIER-STOKES EQUATIONS

Tony W. H. Sheu[1,3], Neo S. C. Kao[1], P. H. Chiu[1], and C. S. Lin[2,3]

[1]*Department of Engineering Science and Ocean Engineering, National Taiwan University, Taipei, Taiwan, Republic of China*

[2]*Department of Mathematics, Nationa Taiwan University, Taipei, Taiwan, Republic of China*

[3]*Taida Institute of Mathematical Science (TIMS), National Taiwan University, Taipei, Taiwan, Republic of China*

In this article we develop a computationally stable and dispersively accurate convective scheme for the incompressible Navier-Stokes equations predicted in non-staggered grids. To enhance the convective stability and improve the dispersion accuracy, the convective terms are approximated by conducting the dispersion analysis to minimize dispersion relation error and Fourier stability analysis. To validate the proposed third-order-accurate two-dimensional numerical scheme, we solve four problems that are all amenable to exact solutions and the lid-driven cavity problem investigated at high Reynolds numbers. Results with good rates of convergence are obtained for the scalar and Navier-Stokes problems.

1. INTRODUCTION

When solving the practically and academically important scalar transport equation at high Peclet numbers and Navier-Stokes equations at high Reynolds numbers, it is essential to eliminate velocity oscillations due to convective instability. As a result, many upwind schemes have been proposed; see, e.g., [1–7]. One theory that can be also adopted to enhance convective stability is to preserve the dispersive nature of the first-order derivative term [8].

Our underlying idea for approximating the convection term is to optimize the discrete dispersion relation. In other words, we aimed to develop a scheme that accommodates almost the same dispersion relation as that of the original first-order derivative term [8]. Application of the theoretical dispersion relation, which can be derived by performing the spatial Fourier transform on the first-order derivative term, helps us to know how the angular frequency is related to the wavenumber

Received 6 April 2011; accepted 9 June 2011.

Address correspondence to Tony W. H. Sheu, Department of Engineering Science and Ocean Engineering, National Taiwan University, No. 1, Sec. 4, Roosevelt Road, Taipei, Taiwan 106, Republic of China. E-mail: twhsheu@ntu.edu.tw

NOMENCLATURE

a,b	convective velocities defined in Eqs. (6), (37)	Pe	Peclet number defined in Eq. (41)
c	reaction coefficient defined in Eqs. (6), (37)	Re	Reynolds number ($\equiv \rho u_\infty L/\mu$)
f	force per unit volume	u_∞	reference velocity
k	diffusion coefficient defined in Eqs. (6), (37)	γ_i	modified wavenumber defined in Eq. (25)
k_m	wave-number defined in Eq. (40	λ_i	Lagrangian multipliers defined in Eq. (26)
L	characteristic length	v	Courant number defined in Eq. (41)
n	unit outward normal vector	ρ	fluid density

of the spatial variable [9]. The resulting dispersiveness, dissipation, group, and phase velocities for each wave component supported by the first-order derivative term can be well modeled [10]. In light of the above we conduct in this article the standard modified equation analysis, which involves performing the truncated Taylor series, together with the Fourier transform analysis [11], which enables us to derive the same or almost the same discrete dispersion relation as the original partial differential equation, in the process of approximating the convective terms.

This article is organized as follows. Section 2 presents the investigated primitive-variable Navier-Stokes equations. This is followed by presenting a compact scheme for approximation of the pressure gradient term to avoid the notorious even–odd oscillations in nonstaggered grids. Section 4 describes the two-dimensional upwind scheme for the approximation of the first-order derivative terms. Section 5 presents the dispersion and Fourier (or von Neumann) stability analyses for the proposed discretization scheme. Section 6 shows the computed results to validate the proposed upwinding scheme. In Section 7 we give some concluding remarks.

2. WORKING EQUATIONS

In this study we aimed to solve the incompressible Navier-Stokes equations, which are cast in the pair of primitive variables ($\underline{u}$, p) in Ω:

$$\nabla \cdot \underline{u} = 0 \tag{1}$$

$$\frac{\partial \underline{u}}{\partial t} + \underline{u} \cdot \nabla \underline{u} = -\nabla p + \frac{1}{\mathrm{Re}} \nabla^2 \underline{u} + \underline{f} \tag{2}$$

Given an initial divergence-free velocity field, the velocity vector $\underline{u}$ and pressure p will be sought subject to the velocity boundary condition. In the above, the length has been normalized by L, the velocity components by u_∞, the time by L/u_∞, and the pressure by ρu_∞^2, where ρ denotes the constant fluid density. The Reynolds number Re is $u_\infty L/\nu$, which is the outcome of the above normalization of equations.

Two momentum equations in (2) can be solved together with the constraint equation (1) for unconditionally ensuring incompressibility. The resulting matrix system will unfortunately become less conditioning and the solutions ($\underline{u}$, p) for the elliptic-parabolic nonlinear equations (1)–(2) are very difficult to converge using the computationally less expensive iterative solvers [12]. In addition, the required peripheral storage for the matrix equation may exceed our availability. These

drawbacks commonly encountered in the mixed formulation prompted the current pressure Poisson equation approach [13].

Within this segregated analysis framework, the equation for p needs to be derived to replace the divergence-free equation (1). By applying a divergence operator on Eq. (2), we can get the following Poisson equation for p in Ω:

$$\nabla^2 p = \nabla\left(-\frac{\partial \underline{u}}{\partial t} + \frac{1}{\mathrm{Re}}\nabla^2 \underline{u} - \underline{u}\cdot\nabla\underline{u} + \underline{f} \right) \tag{3}$$

In other words, we can consider the above Poisson equation as the incompressibility condition. In this segregated approach, difficulty arises from the necessity of specifying a pressure boundary value for Eq. (3) in nonstaggered grids. The reason is that no pressure boundary condition needs to be specified when solving the primitive-variable equations (1) and (2). In addition, calculation of p from the above Poisson equation is also computationally expensive.

3. DISCRETIZATION OF THE PRESSURE GRADIENT TERM IN NONSTAGGERED GRIDS

Discretization of the vector equation (2) in nonstaggered grids has been well known to yield oscillations arising from the even–odd decoupling. Elimination of such a pressure mode in staggered grids will, however, increase the programming complexity and may consume much more computational time. This is our motivation of discretizing Eq. (2) in a domain where velocities and pressure are stored at the same point. In the currently adopted nonstaggered mesh, the pressure gradient term ∇p needs to be properly approximated to avoid spurious pressure oscillations.

Our strategy behind eliminating the even–odd decoupling problem in nonstaggered grids is to take the nodal value of $p_{i,j}$ into account when approximating the pressure gradient term at an interior node (i,j) [14]. Instead of explicitly approximating the pressure gradient term, the value of $\partial p/\partial x|_{i,j}$ will be calculated implicitly along with the two adjacent values of $\partial p/\partial x|_{i\pm 1,j}$. Define $F_{i,j}$ as

$$F_{i,j} = h\frac{\partial p}{\partial x}\Big|_{ij} \tag{4}$$

where h denotes the constant grid size. The method adopted in this study to calculate $F_{i,j}$ implicitly is as follows:

$$\begin{aligned} c_1 F_{i+1,j} + c_2 F_{i,j} + c_3 F_{i-1,j} = {} & c_4\left(p_{i+2,j} - p_{i+1,j} \right) + c_5\left(p_{i+1,j} - p_{i,j} \right) \\ & + c_6\left(p_{i,j} - p_{i-1,j} \right) + c_7\left(p_{i-1,j} - p_{i-2,j} \right) \end{aligned} \tag{5}$$

The above seven undetermined coefficients will be determined by using the Taylor series expansion method. We start with expanding $F_{i\pm 1,j}$ in Taylor series with respect to $F_{i,j}$, and $p_{i\pm 1,j}$ and $p_{i\pm 2,j}$ with respect to $p_{i,j}$. This is followed by substituting these expansion equations into Eq. (5) to get a simultaneous set of algebraic equations that enables us to uniquely determine the seven introduced coefficients. We set $c_1 = c_3$ since p is governed by the elliptic Poisson equation (3). As a result,

the introduced coefficients can be determined as $c_1 = 1/5$, $c_2 = 3/5$, $c_4 = 1/60$, $c_5 = 29/60$, $c_6 = 29/60$, and $c_7 = 1/60$.

In the derivation of the working equation for F_{ij} at the point that is immediately adjacent to the right boundary (for example), we can employ Eq. (5) in the $c_1 = c_4 = c_5 = 0$ limiting condition. According to Eq. (5), the values of F_{ij} $(2 \le i \le j_{\max} - 1)$ can be calculated using a computationally less expensive tridiagonal matrix solver.

4. DEVELOPMENT OF THE TWO-DIMENSIONAL CONVECTION SCHEME

We use the constant-coefficient convection-diffusion equation $\phi_t + a\phi_x + b\phi_y - k\nabla^2\phi + c\phi = f$ to describe our proposed advection scheme. Discretization of this scalar equation is started with approximating ϕ_t by the first-order-accurate Euler scheme to get the following semi-discretization equation:

$$\frac{\phi^{n+1} - \phi^n}{\Delta t} + a\,\phi_x + b\,\phi_y - k\nabla^2\phi = f \tag{6}$$

In this study, the standard second-order-accurate central differencing scheme is employed for approximation of the diffusion term.

In the grid system schematic in Figure 1, the first-order spatial derivative terms shown in (6) will be approximated at $\Delta x = \Delta y = h$. Taking ϕ_x as an example, its value at the reference point 5 can be approximated as follows for the

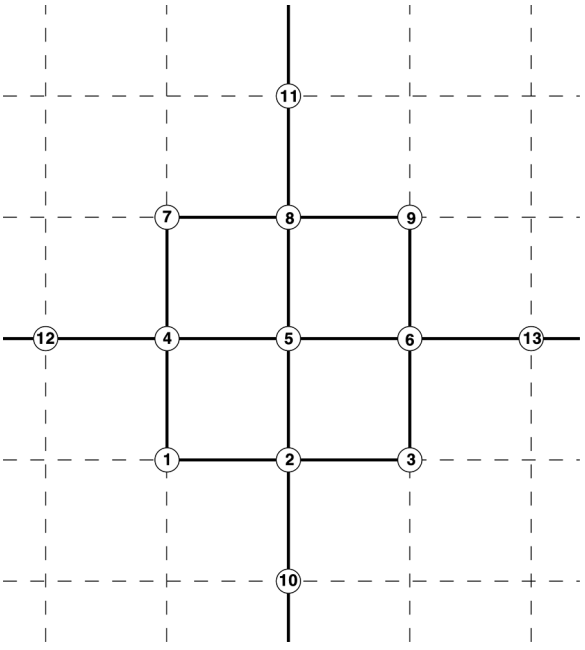

Figure 1. Schematic of the 13-grid stencil.

case with $a > 0$,

$$\begin{aligned}\phi_x(i,j) \simeq \frac{1}{h}(&a_1\,\phi_{i-1,j-1} + a_2\,\phi_{i,j-1} + a_3\,\phi_{i+1,j-1} + a_4\,\phi_{i-1,j} + a_5\,\phi_{i,j} + a_6\,\phi_{i+1,j} \\ &+ a_7\,\phi_{i-1,j+1} + a_8\,\phi_{i,j+1} + a_9\,\phi_{i+1,j+1} + a_{10}\,\phi_{i,j-2} + a_{11}\,\phi_{i,j+2} \\ &+ a_{12}\,\phi_{i-2,j})\end{aligned} \tag{7}$$

and for the case with $a < 0$,

$$\begin{aligned}\phi_x(i,j) \simeq \frac{1}{h}(&a_1\,\phi_{i-1,j-1} + a_2\,\phi_{i,j-1} + a_3\,\phi_{i+1,j-1} + a_4\,\phi_{i-1,j} + a_5\,\phi_{i,j} + a_6\,\phi_{i+1,j} \\ &+ a_7\,\phi_{i-1,j+1} + a_8\,\phi_{i,j+1} + a_9\,\phi_{i+1,j+1} + a_{10}\,\phi_{i,j-2} + a_{11}\,\phi_{i,j+2} + a_{13}\,\phi_{i+2,j})\end{aligned} \tag{8}$$

By applying the Taylor series expansions for $\phi_{i\pm1,\,j}$, $\phi_{i-2,j}$, $\phi_{i,\,j\pm1}$, $\phi_{i,\,j\pm2}$, $\phi_{i\pm1,\,j\pm1}$, we can eliminate the 11 leading error terms with ϕ, ϕ_x, ϕ_y, ϕ_{xx}, ϕ_{xy}, ϕ_{yy}, ϕ_{xxy}, ϕ_{xyy}, ϕ_{xxx}, ϕ_{yyy}, and ϕ_{xxyy} shown in the resulting modified equation to get the following system of algebraic equations:

$$a_1 + a_2 + a_3 + a_4 + a_5 + a_6 + a_7 + a_8 + a_9 + a_{10} + a_{11} + a_{12} = 0 \tag{9}$$

$$-a_1 + a_3 - a_4 + a_6 - a_7 + a_9 - 2a_{12} - 1 = 0 \tag{10}$$

$$-a_1 - a_2 - a_3 + a_7 + a_8 + a_9 - 2a_{10} + 2a_{11} = 0 \tag{11}$$

$$a_1 + a_3 + a_4 + a_6 + a_7 + a_9 + 4a_{12} = 0 \tag{12}$$

$$a_1 - a_3 - a_7 + a_9 = 0 \tag{13}$$

$$a_1 + a_2 + a_3 + a_7 + a_8 + a_9 + 4a_{10} + 4a_{11} = 0 \tag{14}$$

$$-a_1 - a_3 + a_7 + a_9 = 0 \tag{15}$$

$$-a_1 + a_3 - a_7 + a_9 = 0 \tag{16}$$

$$-a_1 + a_3 - a_4 + a_6 - a_7 + a_9 - 8a_{12} = 0 \tag{17}$$

$$a_1 + a_2 + a_3 + a_7 + a_8 + a_9 + 4a_{10} + 4a_{11} = 0 \tag{18}$$

$$-a_1 - a_3 + a_7 + a_9 = 0 \tag{19}$$

One more algebraic equation is needed so as to uniquely determine the coefficients a_1–a_{12} shown in (7).

When convection highly dominates diffusion, it is desirable to get a better relation between the angular frequency of the wave and the wavenumber of the spatial variable. To effectively suppress the convective instability generated in the course of approximating ϕ_x [15], the right-hand side of (7) is made to have nearly the same Fourier transform in space as the original partial derivative shown in the left-hand

side of (7) [15–17]. We define first the following Fourier transform and then its inverse for $\phi(x, y)$ in the domain of two space dimensions (x, y) as follows:

$$\tilde{\phi}(\alpha, \beta) = \frac{1}{(2\pi)^2} \int_{-\infty}^{+\infty} \int_{-\infty}^{+\infty} \phi(x, y)\, e^{-\mathbf{i}(\alpha x + \beta y)}\, dx\, dy \tag{20}$$

$$\phi(x, y) = \int_{-\infty}^{+\infty} \int_{-\infty}^{+\infty} \tilde{\phi}(\alpha, \beta)\, e^{\mathbf{i}(\alpha x + \beta y)}\, d\alpha\, d\beta \tag{21}$$

By performing the Fourier transform on the terms shown in both sides of (7), we get the first component of the actual wavenumber vector $\underline{\alpha} = (\alpha, \beta)$:

$$\begin{aligned} \alpha \simeq \frac{-\mathbf{i}}{h} (& a_1\, e^{-\mathbf{i}(\alpha h + \beta h)} + a_2\, e^{-\mathbf{i}\beta h} + a_3\, e^{\mathbf{i}(\alpha h - \beta h)} + a_4\, e^{-\mathbf{i}\alpha h} + a_5 + a_6\, e^{\mathbf{i}\alpha h} \\ & + a_7\, e^{-\mathbf{i}(\alpha h - \beta h)} + a_8\, e^{\mathbf{i}\beta h} + a_9\, e^{\mathbf{i}(\alpha h + \beta h)} + a_{10}\, e^{\mathbf{i}(-\beta 2h)} \\ & + a_{11}\, e^{\mathbf{i}(\beta 2h)} + a_{12}\, e^{\mathbf{i}(-\alpha 2h)}) \end{aligned} \tag{22}$$

For the sake of accuracy, the first effective wavenumber shown in $\underline{\tilde{\alpha}} = (\tilde{\alpha}, \tilde{\beta})$ can be regarded as the right-hand side of (22) [8]:

$$\begin{aligned} \tilde{\alpha} = \frac{-\mathbf{i}}{h} (& a_1\, e^{-\mathbf{i}(\alpha h + \beta h)} + a_2\, e^{-\mathbf{i}\beta h} + a_3\, e^{\mathbf{i}(\alpha h - \beta h)} + a_4\, e^{-\mathbf{i}\alpha h} + a_5 + a_6\, e^{\mathbf{i}\alpha h} + a_7\, e^{-\mathbf{i}(\alpha h - \beta h)} \\ & + a_8\, e^{\mathbf{i}\beta h} + a_9\, e^{\mathbf{i}(\alpha h + \beta h)} + a_{10}\, e^{\mathbf{i}(-\beta 2h)} + a_{11}\, e^{\mathbf{i}(\beta 2h)} + a_{12}\, e^{\mathbf{i}(-\alpha 2h)}) \end{aligned} \tag{23}$$

where $\mathbf{i} = \sqrt{-1}$. Similarly, the modified wavenumber $\bar{\beta}$ can be derived as

$$\begin{aligned} \tilde{\beta} = \frac{-\mathbf{i}}{h} (& b_1\, e^{-\mathbf{i}(\alpha h + \beta h)} + b_2\, e^{-\mathbf{i}\beta h} + b_3\, e^{\mathbf{i}(\alpha h - \beta h)} + b_4\, e^{-\mathbf{i}\alpha h} + b_5 + b_6\, e^{\mathbf{i}\alpha h} \\ & + b_7\, e^{-\mathbf{i}(\alpha h - \beta h)} + b_8\, e^{\mathbf{i}\beta h} + b_9\, e^{\mathbf{i}(\alpha h + \beta h)} + b_{10}\, e^{\mathbf{i}(-\beta 2h)} \\ & + b_{11}\, e^{\mathbf{i}(\beta 2h)} + b_{12}\, e^{\mathbf{i}(-\alpha 2h)}) \end{aligned} \tag{24}$$

We intend to make $\tilde{\alpha}$ to be equal to $\tilde{\alpha}$ by minimizing $|\alpha h - \tilde{\alpha} h|^2$ (or its integral E) in the following weak sense [8, 9, 15]:

$$E = \int_{-\pi/2}^{\pi/2} \int_{-\pi/2}^{\pi/2} |\alpha h - \tilde{\alpha} h|^2\, d(\alpha h)\, d(\beta h) = \int_{-\pi/2}^{\pi/2} \int_{-\pi/2}^{\pi/2} |\, \mathbf{i}\gamma_1 - \tilde{\gamma}_1\, |^2\, d\gamma_1\, d\gamma_2 \tag{25}$$

where $(\gamma_1, \gamma_2) = (\alpha h, \beta h)$ are the modified wavenumbers along the x and y directions, respectively. Minimization of E is not arbitrary but is rather subjecte to the 11 constraint equations shown respectively in (9)–(19). A proper determination of coefficients a_1–a_{12} should, as a result, take these constraint equations into consideration. This requirement prompts us to minimize another real function $\bar{F}$, which is given below:

$$\bar{F}(a_1, a_2, \ldots, a_{12}) = E + \lambda_1 \cdot (9) + \lambda_2 \cdot (10) + \cdots + \lambda_{10} \cdot (18) + \lambda_{11} \cdot (19) \tag{26}$$

In the above, λ_1–λ_{11} are known as the Lagrangian multipliers to be determined.

By performing $\partial\bar{F}/\partial\lambda_i = 0 (i = 1-11)$, one can rederive the algebraic equations shown in (9)–(19). To get the global/local extreme value of $\bar{F}$, we perform $\partial\bar{F}/\partial a_i = 0 (i = 1-4, \text{and } 6-12)$. The resulting 11 algebraic equations enable us to uniquely express the Lagrangian multipliers λ_1–λ_{11}, which are summarized in the Appendix, in terms of a_5. Derivation of algebraic equations for the introduced coefficients is followed by employing equations (9)–(19) to rewrite a_1–a_4 and a_6–a_{12} in terms of a_5, where the nodal point 5 is the reference node for ϕ_x shown in (7). As a consequence, one can express the functional expression of $\bar{F}(a_5)$ as follows:

$$\bar{F}(a_5) = \left(-\frac{160}{27}\pi + \frac{35}{18}\pi^2\right)a_5^2 + \left(\frac{28}{27}\pi + \frac{128}{9} - \frac{67}{36}\pi^2\right)a_5 + \frac{93}{16}\pi^2 + \frac{\pi^4}{12} - \frac{128}{9} \tag{27}$$

The value of $\bar{F}(a_5)$ can thus be minimized by enforcing $\partial\bar{F}/\partial a_5 = 0$, thereby yielding the following algebraic equation:

$$\left(-\frac{320}{27}\pi + \frac{35}{9}\pi^2\right)a_5 + \frac{28\pi}{27} + \frac{128}{9} - \frac{67\pi^2}{36} = 0 \tag{28}$$

We can then use Eq. (28) together with Eqs. (9)–(19) to uniquely determine the coefficients a_1–a_{12}, which are shown below.

$$a_1 = a_3 = a_7 = a_9 = 0 \tag{29}$$

$$a_2 = a_8 = \frac{512 + 3\pi^2 - 176\pi}{10\pi(-64 + 21\pi)} \tag{30}$$

$$a_4 = -1 \tag{31}$$

$$a_6 = \frac{1}{3} \tag{32}$$

$$a_5 = \frac{-1536 + 201\pi^2 - 112\pi}{20\pi(-64 + 21\pi)} \tag{33}$$

$$a_{10} = a_{11} = -\frac{512 + 3\pi^2 - 176\pi}{40\pi(-64 + 21\pi)} \tag{34}$$

$$a_{12} = \frac{1}{6} \tag{35}$$

Note that the value of $\partial^2\bar{F}/\partial a_5^2$ is larger than zero at $a_5 = 0.77368586$. As a result, $\bar{F}$ plotted in Figure 2 has a local minimum at the value of a_5.

Having derived the 12 coefficients a_1–a_{12}, the modified equation for ϕ_x can be shown to have third-order spatial accuracy.

$$\begin{aligned}\phi_x \simeq\ & 0.0833h^3\phi_{xxxx} + 0.0456h^3\phi_{yyyy} - 0.0333h^4\phi_{xxxxx} \\ & + 0.0138h^5\phi_{xxxxxx} + \cdots + \text{H.O.T.}\end{aligned} \tag{36}$$

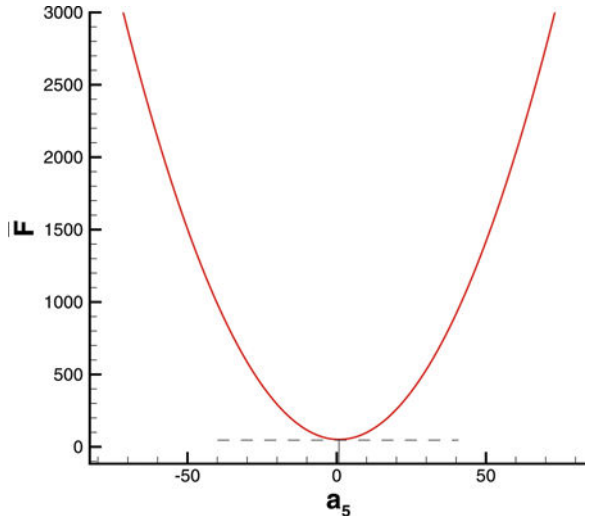

Figure 2. Plot of F, defined in (27) or (28), against a_5 (color figure available online).

For the case of $\bar{b} > 0$, we can similarly derive $b_4 = b_6 = a_2$, $b_2 = a_4$, $b_8 = a_6$, $b_{12} = b_{13} = a_{10}$ and $b_j = a_j$ $(j = 1, 3, 5, 7, 9)$. The modified equation derived in the 13-point stencil for ϕ_y is $\phi_y \simeq 0.0833h^3\,\phi_{yyyy} + 0.0456h^3\phi_{xxxx} - 0.0333h^4\phi_{yyyyy} + 0.0138h^5\phi_{yyyyyy} + \ldots + \text{H.O.T.}$

5. FUNDAMENTAL ANALYSIS OF THE SCHEME

5.1. Dispersion Analysis

Fundamental study of the proposed two-dimensional scheme for the linear model equation given below will be conducted within the implicit Euler time-stepping framework:

$$\frac{\phi^{n+1} - \phi^n}{\Delta t} + a\ \phi_x + b\ \phi_y - k\nabla^2\phi + c\ \phi = 0 \tag{37}$$

Given the initial condition of ϕ as $\phi(x, y, t = 0) = \exp[\mathbf{i}(\alpha x + \beta y)]$, the exact solution to the above equation can be easily derived in terms of (α, β) as

$$\phi(x, y, t) = \exp\{-[k(\alpha^2 + \beta^2) + c]t\}\exp\{\mathbf{i}[\alpha(x - at) + \beta(y - bt)]\} \tag{38}$$

The proposed discrete equation at an interior point (i, j) is assumed to take the following form:

$$\begin{aligned} &A_1\phi_{i-1,j-1}^{n+1} + A_2\phi_{i,j-1}^{n+1} + A_3\phi_{i+1,j-1}^{n+1} + A_4\phi_{i-1,j}^{n+1} + A_5\phi_{i,j}^{n+1} + A_6\phi_{i+1,j}^{n+1} \\ &\quad + A_7\phi_{i-1,j+1}^{n+1} + A_8\phi_{i,j+1}^{n+1} + A_9\phi_{i+1,j+1}^{n+1} + A_{10}\phi_{i,j-2}^{n+1} + A_{11}\phi_{i,j+2}^{n+1} \\ &\quad + A_{12}\phi_{i-2,j}^{n+1} + A_{13}\phi_{i+2,j}^{n+1} = \phi_{i,j}^{n} \end{aligned} \tag{39}$$

The exact solution to the discrete equation (38), which accounts for the inevitably introduced amplitude and phase errors, is assumed below:

$$\tilde{\phi}(x,y,t) = \exp\left\{-\left[\left(k\alpha^2+\frac{c}{2}\right)\frac{k_r}{\gamma_1^2}+\left(k\beta^2+\frac{c}{2}\right)\frac{k_r}{\gamma_2^2}\right]t\right\} \exp\left\{\mathbf{i}\left[\alpha\left(x-a\frac{k_i}{\gamma_1}t\right)+\beta\left(y-b\frac{k_i}{\gamma_2}t\right)\right]\right\}$$

or

$$\tilde{\phi}(x,y,t) = A\exp(\bar{p}+\mathbf{i}\bar{q})\exp[\mathbf{i}k_m(x+y)] \tag{40}$$

The following equation can be easily derived in terms of $(\gamma_1, \gamma_2)=(\alpha h, \beta h)$, where $\nu_x = a\Delta t/h$, $\nu_y = b\Delta t/h$, $\mathrm{Pe}_x = ah/k$, $\mathrm{Pe}_y = bh/k$, $R_x = ch/a$, and $R_y = ch/b$.

$$-\left\{\left[\left(k\alpha^2+\frac{c}{2}\right)\frac{k_r}{\gamma_1^2}+\left(k\beta^2+\frac{c}{2}\right)\frac{k_r}{\gamma_2^2}\right]+\mathbf{i}\left(\alpha a\frac{k_i}{\gamma_1}+\beta b\frac{k_i}{\gamma_2}\right)\right\}\Delta t$$
$$=-\left\{\left[\left(k\alpha^2+\frac{c}{2}\right)\frac{k_r}{(\alpha h)^2}+\left(k\beta^2+\frac{c}{2}\right)\frac{k_r}{(\beta h)^2}\right]+\mathbf{i}\left(\alpha a\frac{k_i}{\alpha h}+\beta b\frac{k_i}{\beta h}\right)\right\}\Delta t$$

Dispersion analysis of the discrete equation involves substituting the values of $\phi_{i,j}$, $\phi_{i\pm1,j}$, $\phi_{i,j\pm1}$, $\phi_{i\pm2,j}$, $\phi_{i,j\pm2}$, and $\phi_{i\pm1,j\pm1}$, which are calculated from Eq. (38), into Eq. (39). After some algebra, the expressions of k_r and k_i that account for the respective amplitude and phase errors can be derived as

$$k_r = \frac{-\bar{p}}{\left(\frac{\nu_x}{Pe_x}\right)+\left(\frac{\nu_x}{Pe_x}\right)+\frac{1}{2}\left\{\left[\frac{(\nu_x R_x+1)}{\gamma_1^2}\right]+\left[\frac{(\nu_y R_y+1)}{\gamma_2^2}\right]\right\}} \tag{41}$$

$$k_i = \frac{-\bar{q}}{\nu_x+\nu_y} \tag{42}$$

By substituting the exact expressions for $\phi_{i,j}$, $\phi_{i\pm1,j}$, $\phi_{i,j\pm1}$, and $\phi_{i\pm1,j\pm1}$ into Eq. (39), we get the following equation:

$$e^{\bar{p}}\Big(A_1e^{\mathbf{i}(\bar{q}-\bar{x})}+A_2e^{\mathbf{i}(\bar{q}-\gamma_2)}+A_3e^{\mathbf{i}(\bar{q}+\bar{y})}+A_4e^{\mathbf{i}(\bar{q}-\gamma_1)}+A_5e^{\mathbf{i}\bar{q}}+A_6e^{\mathbf{i}(\bar{q}+\gamma_1)}$$
$$+A_7e^{\mathbf{i}(\bar{q}-\bar{y})}+A_8e^{\mathbf{i}(\bar{q}+\gamma_2)}+A_9e^{\mathbf{i}(\bar{q}+\bar{x})}+A_{10}e^{\mathbf{i}(\bar{q}-2\gamma_2)}+A_{11}e^{\mathbf{i}(\bar{q}+2\gamma_2)}$$
$$+A_{12}e^{\mathbf{i}(\bar{q}-2\gamma_1)}+A_{13}e^{\mathbf{i}(\bar{q}+2\gamma_1)}\Big)=1$$

where $\bar{x}=\gamma_1+\gamma_2$ and $\bar{y}=\gamma_1-\gamma_2$. The values of $\bar{q}$ and $\bar{p}$ can be derived respectively from the imaginary and real parts as follows:

$$\bar{q} = \tan^{-1}\frac{n}{m}$$

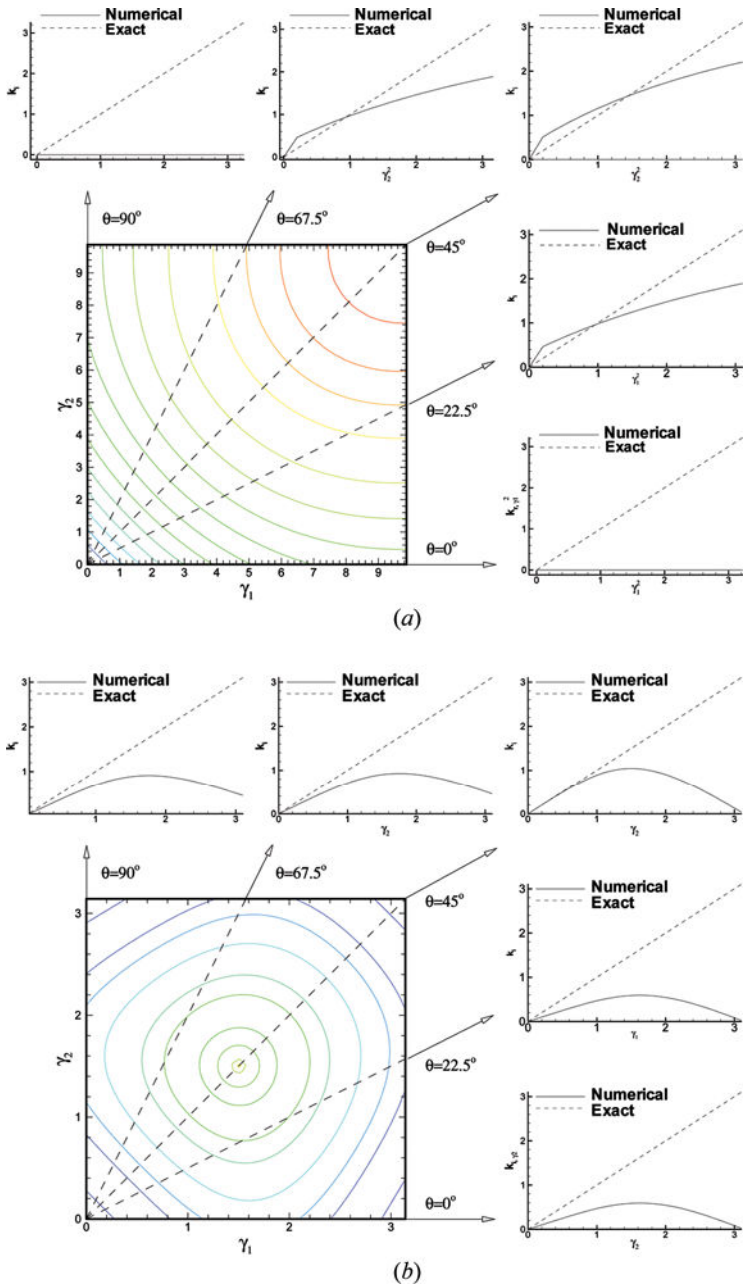

Figure 3. Values of k_r and k_i plotted against (γ_1^2, γ_2^2) and (γ_1, γ_2), respectively, for the proposed scheme considered at $\mathrm{Pe}_x = \mathrm{Pe}_y = 10^3$, $R_x = R_y = 0$, and $\nu_x = \nu_y = 0.2$. Note that the dashed lines represent the exact solutions. (*a*) k_r, (*b*) k_i (color figure available online).

$$\bar{p} = \ln\left(\frac{1}{m\cos\bar{q} + n\sin\bar{q}}\right)$$

In the above, m and n are

$$\begin{aligned} m = {} & (A_1 + A_9)\cos\bar{x} + (A_2 + A_8)\cos\gamma_2 + (A_3 + A_7)\cos\bar{y} + (A_4 + A_6)\cos\gamma_1 \\ & + A_5 + (A_{10} + A_{11})\cos(2\gamma_2) + (A_{12} + A_{13})\cos(2\gamma_1) \\ n = {} & (A_1 - A_9)\sin\bar{x} + (A_2 - A_8)\sin\gamma_2 + (A_3 - A_7)\sin\bar{y} + (A_4 - A_6)\sin\gamma_1 \\ & + (A_{10} - A_{11})\sin(2\gamma_2) + (A_{12} - A_{13})\sin(2\gamma_1) \end{aligned}$$

One can observe from Figure 3, which plots the values of k_r and k_i against (ν_x, ν_y) and (Pe_x, Pe_y) [fixed (R_x, R_y)], that k_i agrees perfectly with its analytic counterpart shown in the line marked by (...) in the small wavenumber range. The larger the wavenumber, the less satisfactory is the predicted phase. In contrast to the plot of k_i, the amplitude error is exhibited even in the small wavenumber range. We also plot in Figure 4 the ratio of the numerical group velocity $C_g[\equiv 1/2(d\omega/d\gamma_1 + d\omega/d\gamma_2)]$ with respect to the analytic wave velocity, which is marked by (...), where $\omega[\equiv(a\,\alpha\,k_i/\gamma_1 + b\,\beta\,k_i/\gamma_2)]$ is obtained from the dispersion equation.

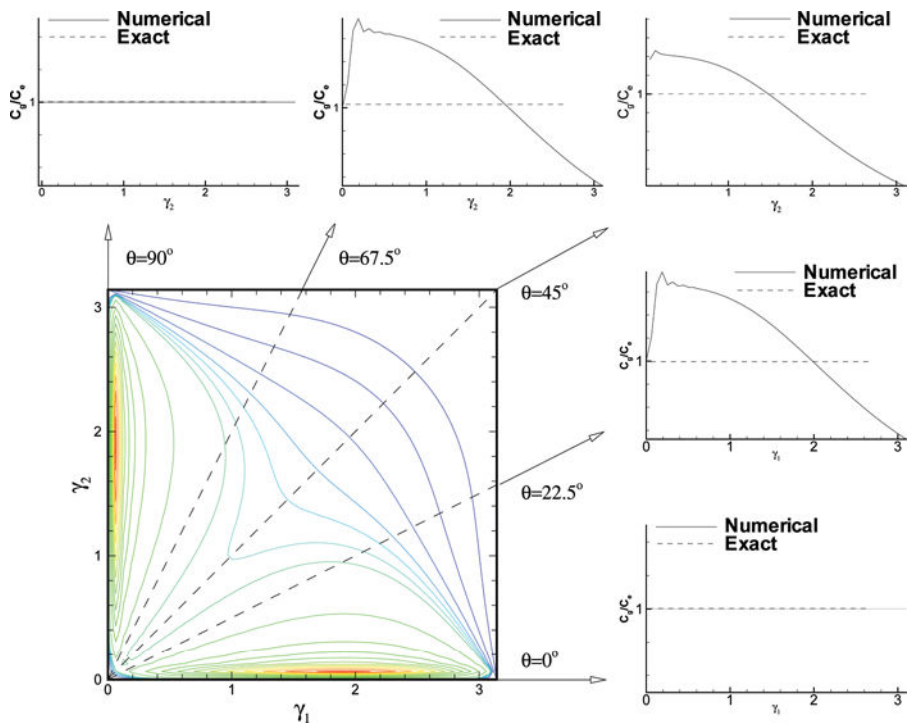

Figure 4. Group velocity ratio C_g/C_e plotted against modified wavenumber (γ_1, γ_2) at $\mathrm{Pe}_x = \mathrm{Pe}_y = 10^3$, $R_x = R_y = 0$, and $\nu_x = \nu_y = 02$ (color figure available online).

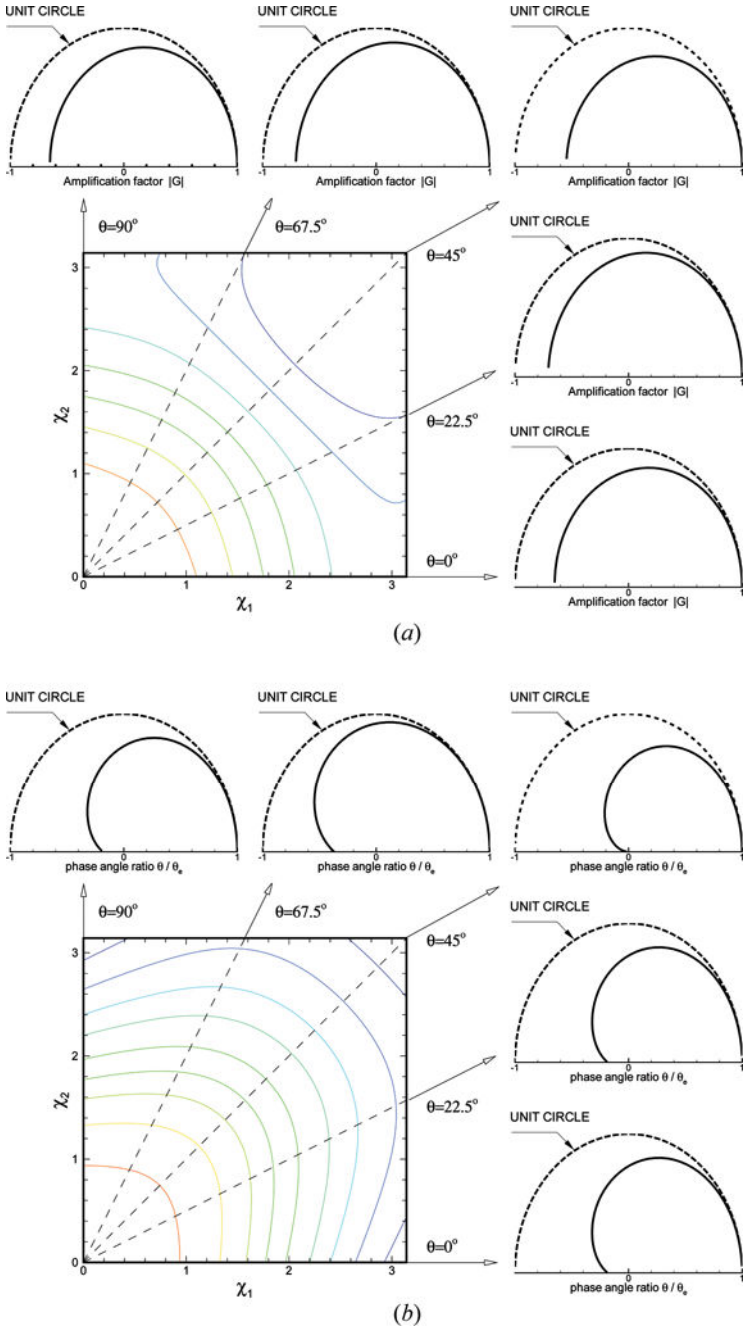

Figure 5. Values of $|G|$ and θ/θ_e plotted against (γ_1, γ_2 at $\mathrm{Pe}_x = \mathrm{Pe}_y = 10^3$, $R_x = R_y = 0$, and $v_x = v_y = 0.2$. (*a*) Amplification factor $|G|$. (*b*) Phase angle ratio θ/θ (color figure available online).

5.2. Fourier or von Neumann Stability Analysis

Fourier (or, von Neumann) stability analysis [18] is now conducted. Let $\chi_x = \chi_y = (2\pi m/2L)h$ ($m = 0, 1, 2, 3, \ldots, M$), h be the grid size, and $2L$ be the period of fundamental frequency ($m = 1$). The amplification factor $G(\equiv \phi_{i,j}^{n+1}/\phi_{i,j}^{n})$ is derived as

$$G = e^{\bar{p}}(\cos\bar{q} + \mathbf{i}\sin\bar{q}) \tag{43}$$

We can see from Figure 5*a* that the magnitude of $|G|$ is always smaller than one. The proposed scheme for Eq. (6) is, thus, classified to be unconditionally stable.

The amplification factor shown in (43) can be also written in the exponential form as $G = |G|\, e^{i\theta}$, where θ is the phase angle,

$$\theta = \tan^{-1}\left|\frac{\mathrm{Im}(G)}{\mathrm{Re}(G)}\right|$$

The relative phase shift error is expressed as

$$\frac{\theta}{\theta_e} = \frac{\tan^{-1}|\mathrm{Im}(G)/\mathrm{Re}(G)|}{-(\chi_x\nu_x + \chi_y\nu_y)}$$

where θ_e is the exact phase angle. For clearness, θ/θ_e is plotted against the values of (χ_x, χ_y), (ν_x, ν_y), (Pe_x, Pe_y), and (R_x, R_y) in Figure 5*b*.

6. NUMERICAL STUDIES

6.1. Problem Without a Boundary Layer

The steady-state convection-diffusion equation

$$-k\nabla^2\phi + a\phi_x + b\phi_y = f$$

will be solved subject to the Dirichlet-type boundary condition. Given the fixed velocity (a, b) = (1, 10.5) in the flow domain and the boundary data schematic in Figure 6*a*, the analytical solution takes the following form:

$$\phi = \frac{\phi_0}{e^{r+} - e^{r-}} e^{\delta_x/2}\sin(\pi x)(e^{r+y} - e^{r-y})$$

In the above, $\phi_0 = 1$, $\delta_x = uL/\mu$, $\delta_y = vL/\mu$, $L = 1$, $\mu = 1$, and

$$r_{\pm} = \frac{1}{2}\delta_y \pm \frac{1}{2}\sqrt{(\delta_y^2 + 4W)}, \quad W = 4\pi^2 + \delta_x^2/4$$

We plot first the smoothly distributed contour values of ϕ in Figure 6*b*. Good agreement with the exact solution shown in Figure 6*c* for the simulation carried out at $\Delta x = \Delta y = 1/60$ and the theoretical rate of convergence shown in Figure 6*d* demonstrate the applicability of the proposed scheme to solve the convection-diffusion equation.

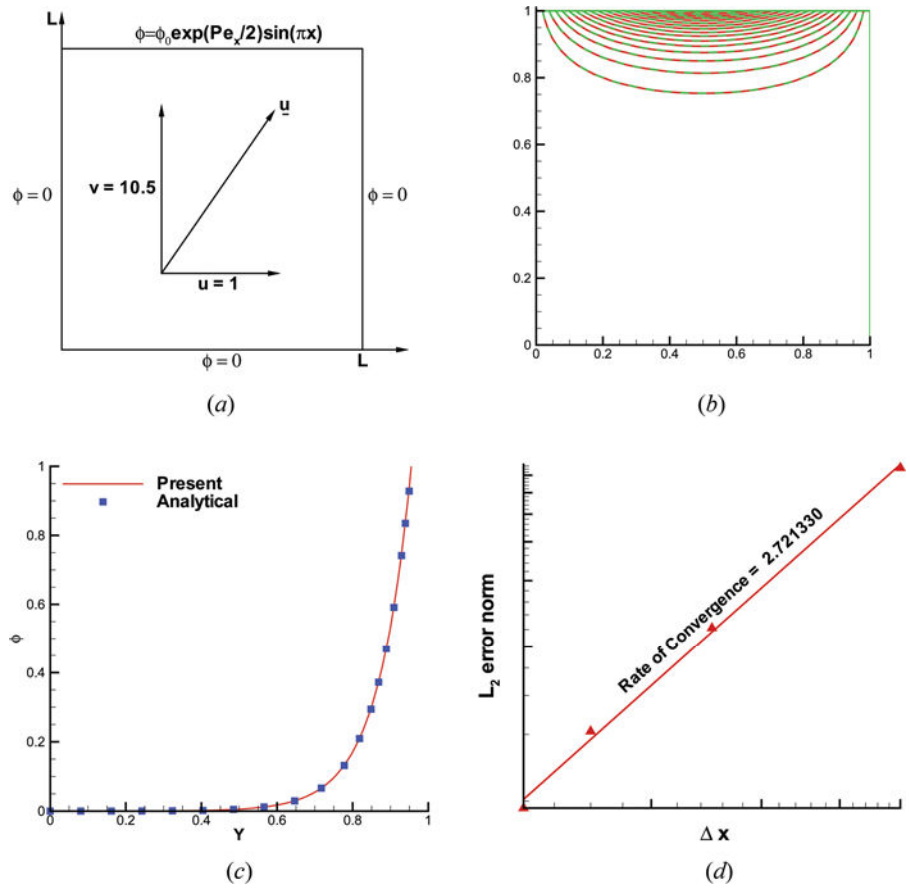

Figure 6. Simulated solutions for the two problems considered in Section 6.1 (*a*) Schematic of the problem (*b*) Predicted solution contours (*c*) Comparison of the computed solution profile $\phi(x = 0.5, y)$ with the analytical solution profile at $x = 0.5$ (*d*) Predicted rate of convergence (color figure available online).

6.2. Problem with a Boundary Layer

Simulation of flow problems that contain the high-gradient solution profile in the physical domain has long been considered as an important topic. For this reason, we investigate the problem schematic in Figure 7, whose solution takes the following boundary-layer form:

$$\phi(x,y) = \frac{\left\{1 - \exp\left[(x-1)\left(\frac{a}{\mu}\right)\right]\right\}}{\left[1 - \exp\left(\frac{-a}{\mu}\right)\right]} \frac{\left\{1 - \exp\left[(y-1)\left(\frac{b}{\mu}\right)\right]\right\}}{\left[1 - \exp\left(\frac{-b}{\mu}\right)\right]}$$

The predicted solution is carried out at $\Delta x = \Delta y = 1/60$. One can clearly see from Figure 8 that nonoscillatory solutions and the associated rate of convergence can be sharply predicted in regions near the boundary. We also tabulated the predicted

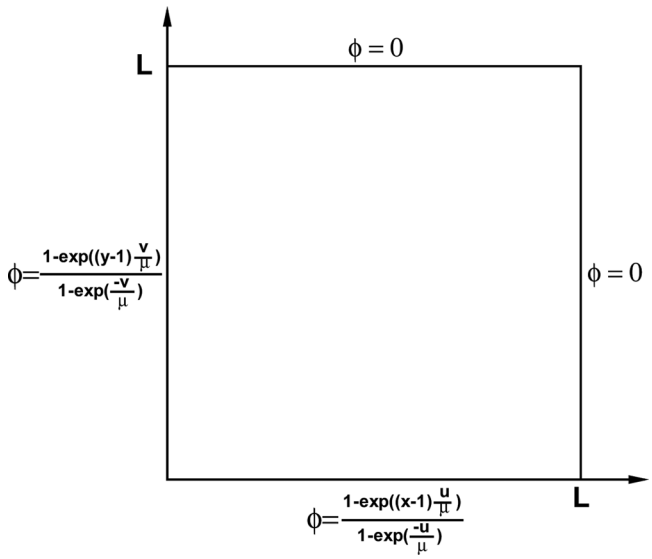

Figure 7. Schematic of the test problem given in Section 6.2.

L_2 error norms in Table 1 to show that the predicted rate of convergence is close to its theoretical rate when solving the problem involving a sharp boundary layer in convection-dominated flow.

6.3. Time-Dependent Convection-Diffusion Problem

The third time-dependent test problem schematic in Figure 9*a* is defined in $\Omega = (-0.5, 0.5) \times (-0.5, 0.5)$. The initial condition we plot in Figure 9*b* is given by

$$\phi(x, y, 0) = \exp\left[-\frac{(x - x_c)^2 + (y - y_c)^2}{2\sigma^2}\right]$$

where (x_c, y_c) is the center of flow rotation and σ is the standard deviation. The exact solution with constant diffusivity coefficient k and rotating velocity field $(a, b) = (-4y, 4x)$ is given by [19]

$$\phi(x, y, t) = \frac{2\sigma^2}{2\sigma^2 + 4kt}\exp\left[-\frac{(\bar{x} - x_c)^2 + (\bar{y} - y_c)^2}{2\sigma^2 + 4kt}\right]$$

where $\bar{x} = x\cos(4t) + y\sin(4t)$, $\bar{y} = -x\sin(4t) + y\cos(4t)$, $x_c = -0.2$, $y_c = 0$, $\sigma = 0.1$, $\Delta x = \Delta y = 1/100$, and $k = 0.01$. The predicted solutions in Figures 9*c*–9*f* are seen to agree excellently with the analytical solution.

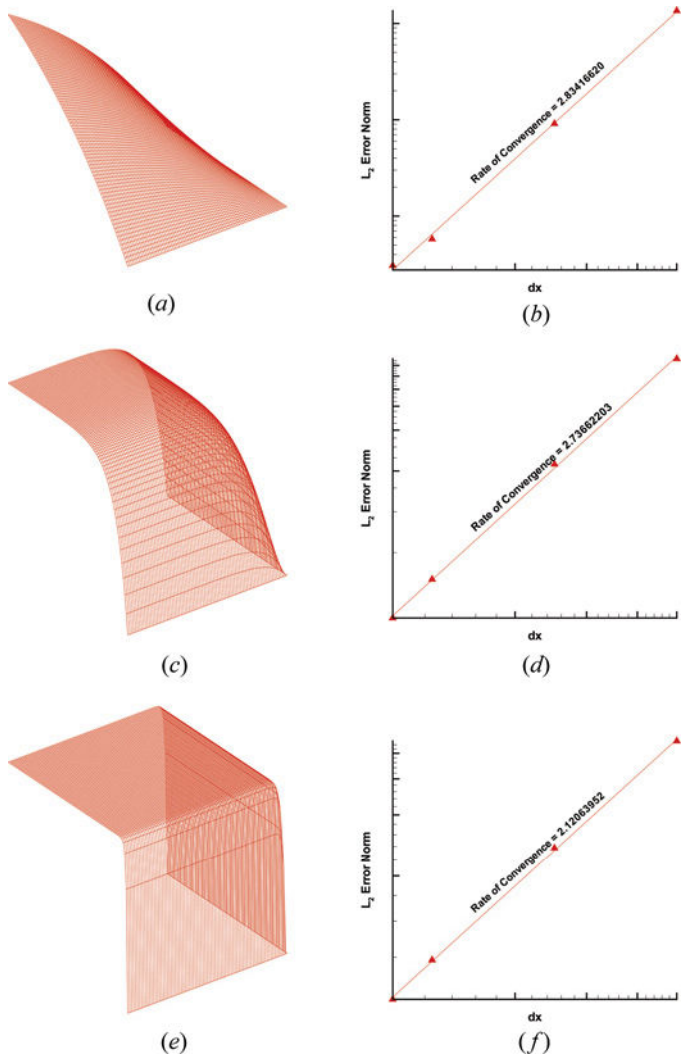

Figure 8. Predicted solutions (*a*), (*c*), (*e*) and rates of convergence (R.O.C.) (*b*), (*d*), (*f*) for the problem considered in Section 6.2. (*a*) $u = v = 1$. (*b*) R.O.C. for $u = v = 1$. (*c*) $u = v = 10$. (*d*) R.O.C. for $u = v = 10$. (*e*) $u = v = 100$. (*f*) R.O.C. for $u = v = 100$ (color figure available online).

Table 1. Predicted L_2-error norms and averaged rate of convergence for the problem given in Section 6.2

Grid sizes	$u = v = 1$	$u = v = 10$	$u = v = 100$
20×20	1.35×10^{-6}	1.34×10^{-3}	4.59×10^{-2}
40×40	9.11×10^{-8}	2.24×10^{-4}	1.37×10^{-2}
80×80	5.78×10^{-9}	3.17×10^{-5}	3.87×10^{-3}
100×100	3.07×10^{-9}	1.64×10^{-5}	2.49×10^{-3}
R. O. C.	2.8341	2.7366	2.1206

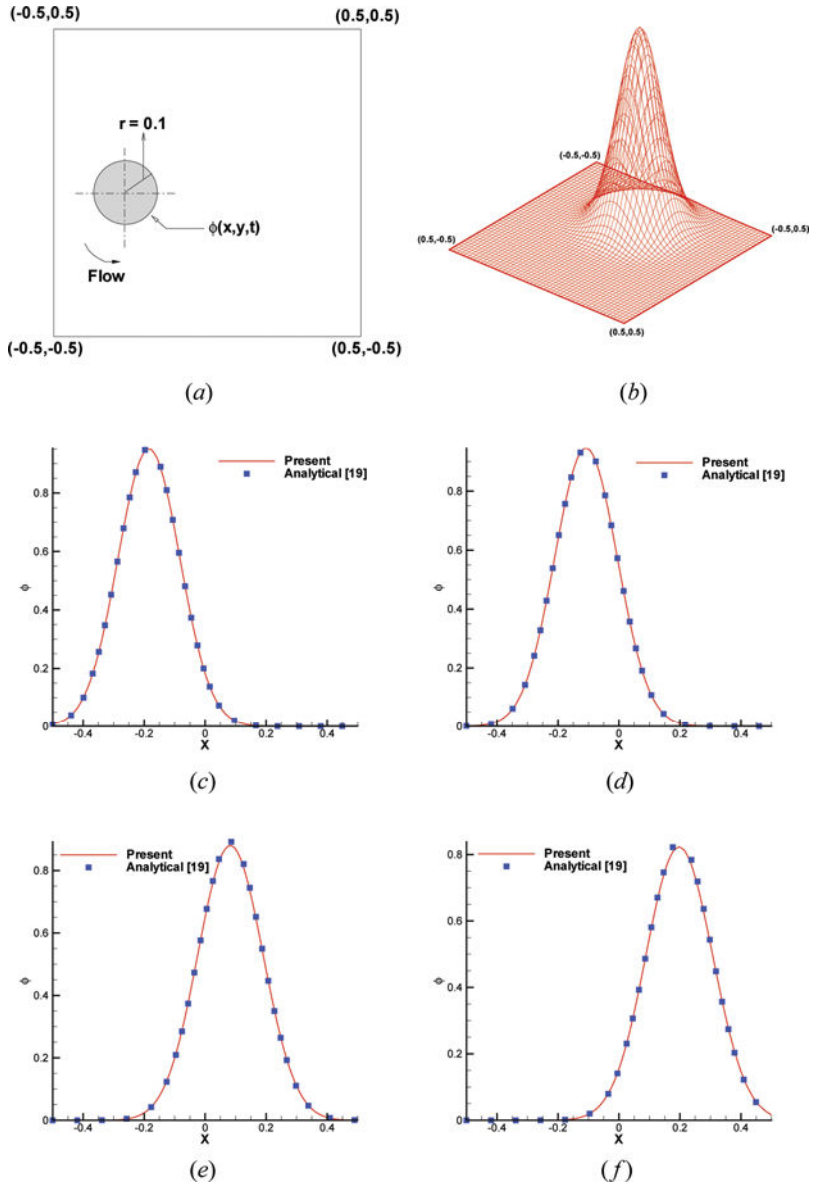

Figure 9. Problem under investigation and solution profiles ϕ computed at different times. (*a*) Schematic of the problem considered in Section 6.3. (*b*) Initial distribution of ϕ. (*c*) $t = 0.1$. (*d*) $t = 0.25$. (*e*) $t = 0.5$. (*f*) $t = 0.75$ (color figure available online).

6.4. Cyclogenisis Problem

We next investigate the cyclogensis problem [20], which describes the mixing of a warm and a cold fluid in $-4 \leq x,\ y \leq 4$. This rotational mixing of two fluids schematic in Figure 10 provides an excellent test of numerical schemes, since the domain

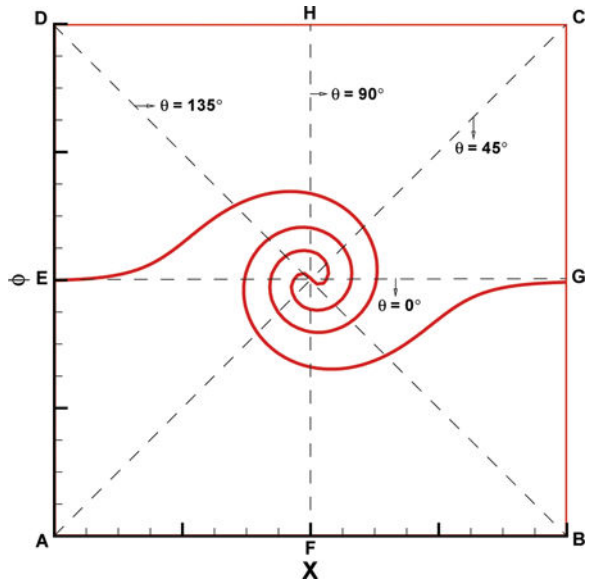

Figure 10. Schematic of the cyclogenesis problem (color figure available online).

of investigation involves both high and low gradients that evolve in space and time. In addition, the following available analytical solution in the limiting case $k = 0$ makes it suitable to validate the scheme:

$$\phi(x, y, t) = -\tan h\left(\frac{y}{2}\cos \omega t - \frac{x}{2}\sin \omega t\right)$$

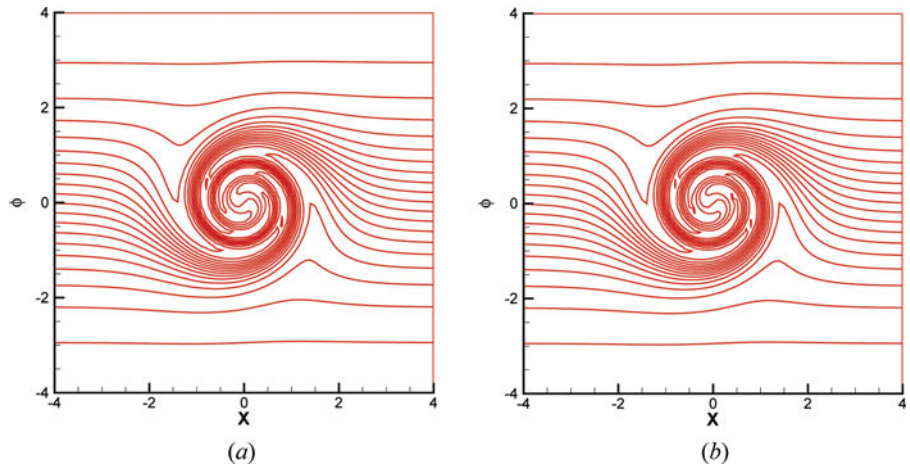

Figure 11. Predicted solutions for the cyclogenesis problem considered in Section 6.4. (*a*) Exact solution. (*b*) Numerical solution (color figure available online).

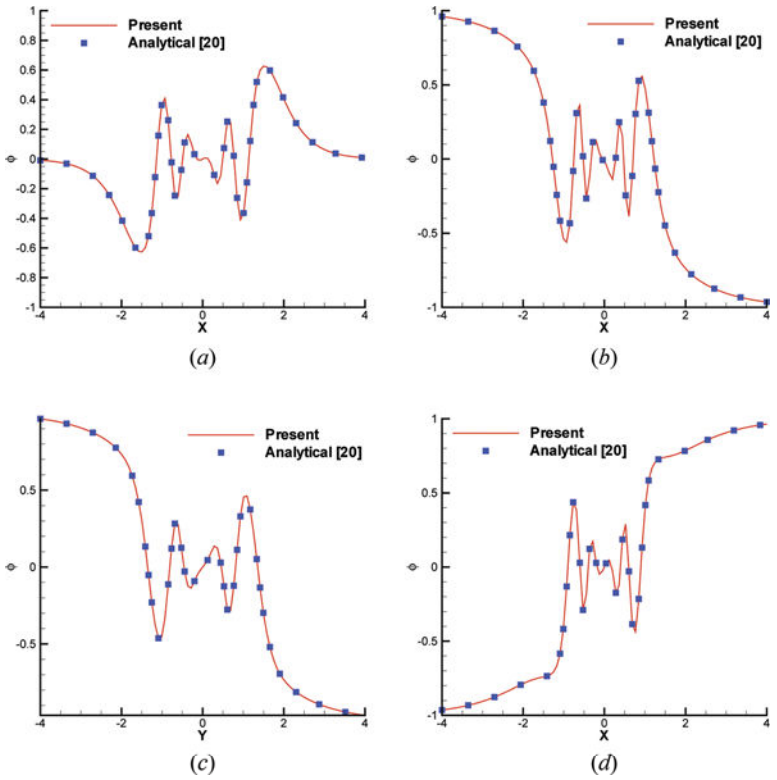

Figure 12. Comparison of predicted and exact solutions for the cyclogenesis problem. (*a*) Solution along the line $\overline{EG}$. (*b*) Solution along the line $\overline{FH}$. (*c*) Solution along the line $\overline{AC}$. (*d*) Solution along the line $\overline{DB}$ (color figure available online).

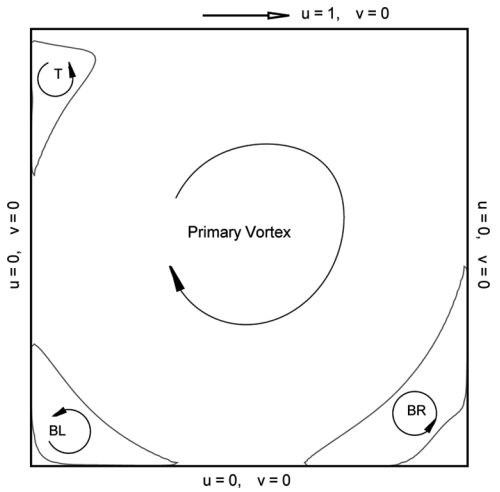

Figure 13. Schematic of the eddy centers in the lid-driven cavity.

where

$$\omega = \frac{v_t}{v_{t_{\max}}}$$
$$v_t = \sec h^2(r)\tanh(r)$$

In the above, ω denotes the rotational frequency and v_t is the tangential velocity at the location that is away from the point (0, 0) with a length r. In the expression of ω, $v_{t_{\max}}$ is the maximum tangential velocity, which is equal to 0.385. The initial condition is given by

$$\phi(x, y, 0) = -\tan h\left(\frac{y}{2}\right)$$

As $t > 0$, the initially prescribed solution will be twisted by the rotational velocity field $u = -\omega y$, $v = \omega x$, thus leading to a rapid change of the solution gradient. The

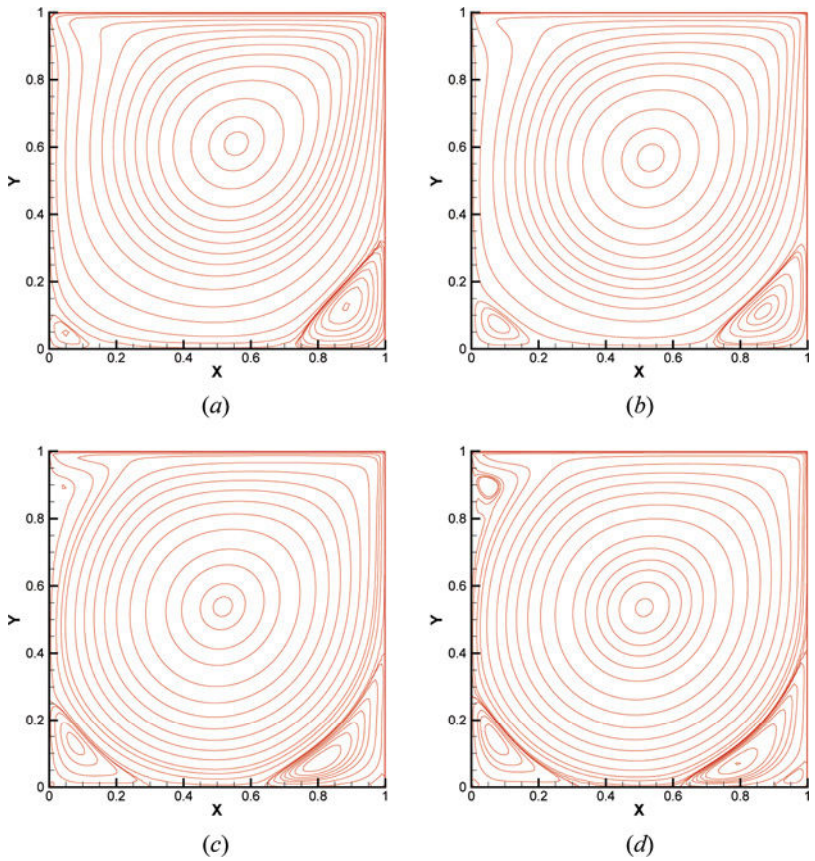

Figure 14. Contours of streamfunction predicted at different Reynolds numbers Re for the lid-driven cavity problem. (a) Re = 400. (*b*) Re = 1,000. (*c*) Re = 5,000. (*d*) Re = 7,500 (color figure available online).

exact and numerical solutions $\phi(x, y, t=4)$ obtained at $\Delta t = 0.01$ and $\Delta x = \Delta y = 1/100$ are plotted in Figures 11*a* and Figure 11*b*. For the sake of comparison, we plot the solution profiles at four different lines in Figures 12*a*–12*d*. The simulated results are seen to agree excellently with the corresponding exact solutions.

6.5. Lid-Driven Cavity Flow Problem

The lid-driven cavity problem schematic in Figure 13 is investigated in a square with 128×128 nodal points. For comparison proposes, the predicted streamfunction contours in Figure 14 and the velocity profiles $u(0.5, y)$ and $v(x, 0.5)$ in Figure 15 are compared with the steady-state benchmark solutions of U. Ghia [21] at $\mathrm{Re} = 400$, 1,000, 5,000 and 7,500 and Kumar [22] at $\mathrm{Re} = 1{,}000$, 5,000 and 7,500. Because of the extremely good agreement between the simulated and the benchmark mid-sectional velocity profiles and the fairly fast residual reduction plots for $\mathrm{Re} = 5{,}000$, 7,500 and 9,000 in Figure 16–18, we confirm the applicability of using the proposed scheme to conduct high-Reynolds-number flow simulations.

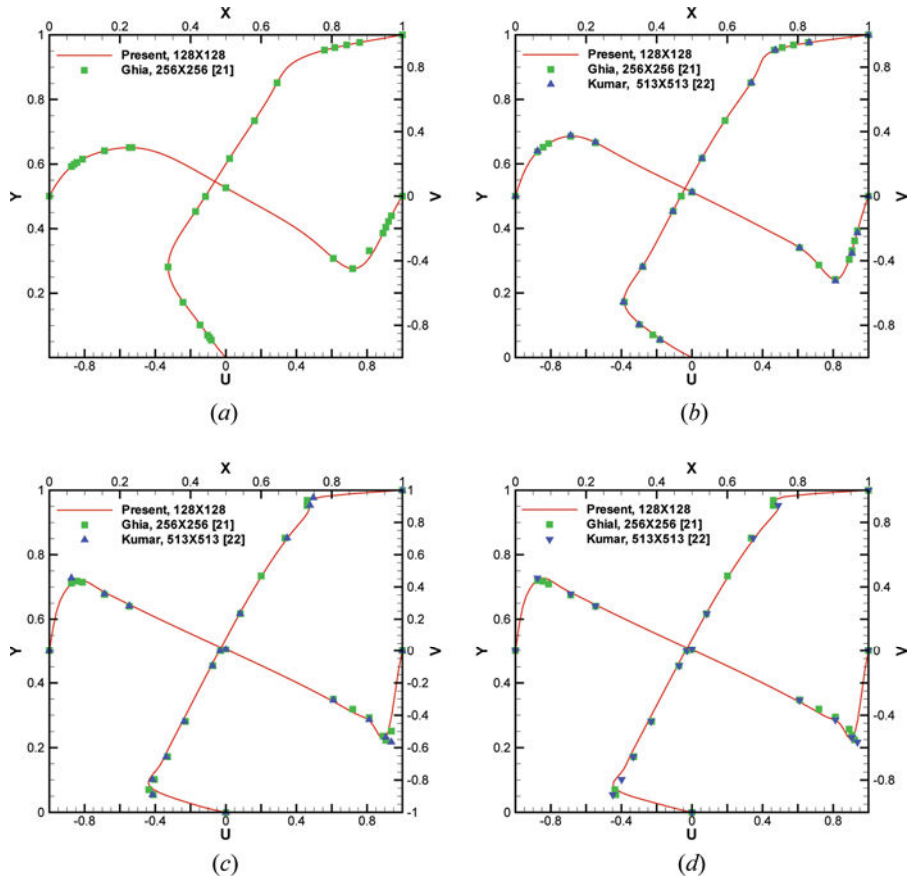

Figure 15. Comparison of velocity profiles $u(0.5, y)$ and $v(x, 0.5)$ predicted at different Reynolds numbers Re. (*a*) $\mathrm{Re} = 400$. (*b*) $\mathrm{Re} = 1{,}000$. (*c*) $\mathrm{Re} = 5{,}000$. (*d*) $\mathrm{Re} = 7{,}500$ (color figure available online).

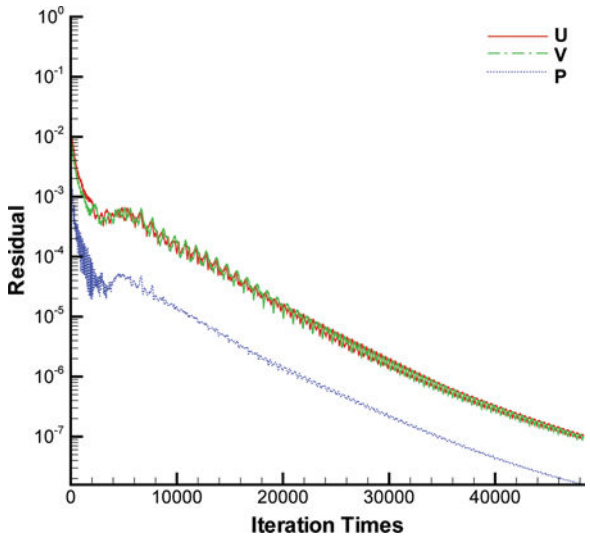

Figure 16. Predicted residual reduction plots for the lid-driven cavity flow simulations for Re = 5,000 (color figure available online).

7. CONCLUDING REMARKS

In this study we have developed a convection scheme to get better dispersive accuracy by minimizing the dispersive error through the introduced Lagrangian multipliers. Theoretical analysis of the upwind scheme for the convection-diffusion

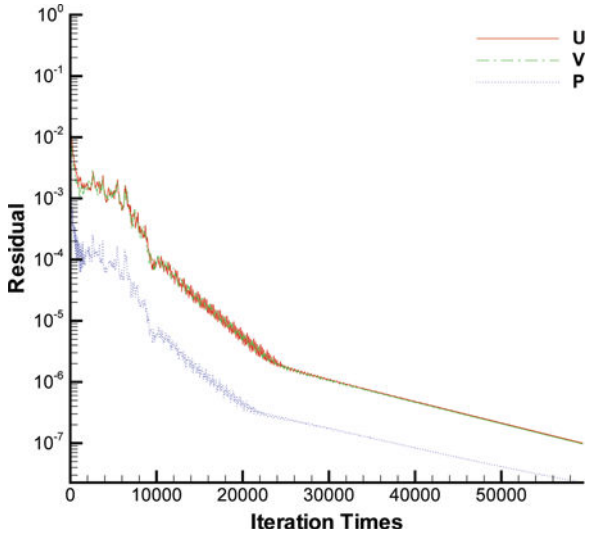

Figure 17. Predicted residual reduction plots for the lid-driven cavity flow simulations for Re = 7,500 (color figure available online).

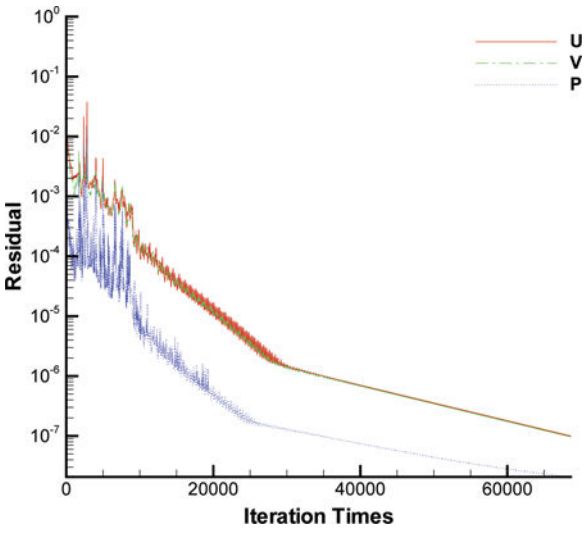

Figure 18. Predicted residual reduction plots for the lid-driven cavity flow simulations for Re = 9,000 (color figure available online).

equation has been performed to get a better understanding of the proposed scheme. Four test problems amenable to exact solutions have been investigated to justify the proposed scheme, which is applicable to predict the problems with smooth as well as sharply varying solutions. The benchmark lid-driven cavity problem investigated at fairly high Reynolds numbers has also been investigated. All the predicted results have good agreement with reliable reference solutions.

REFERENCES

1. D. B. Spalding, A Novel of Finite Difference Formulation for Differential Expressions Involving Both First and Second Derivatives, *Int. J. Numer. Meth. Eng.*, vol. 4, pp. 551–559, 1972.
2. B. P. Leonard, A Stable and Accurate Convective Modelling Procedure Based on Quadratic Upstream Interpolation, *Comput. Meth. Appl. Mech. Eng.*, vol. 19, pp. 5–98, 1979.
3. C. R. Swaminathan and V. R. Voller, Streamline Upwind Scheme For Control-Volume Finite Elements, Part I. Formulations, *Numer. Heat Transfer, B*, vol. 22, pp. 95–107, 1992.
4. G. de Felice, F. M. Denaro, and C. Meola, Multidimensional Single-Step Vector Upwind Schemes for Highly Convective Transport Problems, *Numer. Heat Transfer B*, vol. 23, pp. 425–460, 1993.
5. Y. Li and M. Rudman, Assessment of Higher-Order Upwind Schemes Incorporating FCT for Convection-Dominated Problems, *Numer. Heat Transfer B*, vol. 27, pp. 1–21, 1995.
6. T. W. Sheu, S. F. Tsai, and M. M. T. Wang, Monotone Multidimensional Upwind Finite Element Method for Advection-Diffusion Problems, *Numer. Heat Transfer B*, vol. 29, pp. 325–344, 1996.
7. T. W. H. Sheu, S. F. Tsai, and S. K. Wang, Monotonic, Multidimensional Flux Discretization Scheme For All Peclet Numbers, *Numer. Heat Transfer B*, vol. 31, pp. 441–457, 1997.

8. C. K. W. Tam and J. C. Webb, Dispersion-Relation-Preserving Finite Difference Schemes for Computational Acoustics, *J. Comput. Phys.*, vol. 107, pp. 262–281, 1993.
9. I. A. Abalakin, A. V. Alexandrov, V. G. Bobkov, and T. K. Kozubskaya, High Accuracy Methods, and Software Development In Computational Aeroacoustics, *J. Comput. Meth. Sci. Eng.*, vol. 2, pp. 1–14, 2003.
10. F. Q. Hu, M. Y. Hussaini, and J. L. Manthey, Low-Dissipation and Low-Dispersion Runge-Kutta Schemes for Computational Acoustics, *J. Comput. Phys.*, vol. 124, pp. 177–191, 1996.
11. D. W. Zingg, Comparison of High Accuracy Finite-Diference Methods for Linear Wave Propagation, *SIAM J. Sci. Comput.*, vol. 22, pp. 476–502, 2000.
12. M. M. T. Wang and T. W. H. Sheu, An Element-by-Element BICGSTAB Iterative Method for Three-Dimensional Steady Navier-Stokes Equations, *J. Comput. Appl. Math.*, vol. 79, pp. 147–165, 1997.
13. P. M. Gresho and R. L. Sani, On Pressure Boundary Conditions for the Incompressible Navier-Stokes Equations, *Int. J. Numer. Meth. Fluids*, vol. 7, pp. 1111–1145, 1987.
14. T. W. H. Sheu and R. K. Lin, An Incompressible Navier-Stokes Model Implemented on Nonstaggered Grids, *Numer. Heat Transfer B*, vol. 44, pp. 277–294, 2003.
15. C. Bogry and C. Bailly, A Family of Low Dispersive and Low Dissipative Explicit Schemes for Flow and Noise Computations, *J. Comput. Phys.*, vol. 194, pp. 194–214, 2004.
16. T. K. Sengupta, G. Ganeriwal, and S. De, Analysis of Central and Upwind Compact Schemes, *J. Comput. Phys.*, vol. 192, pp. 677–694, 2003.
17. T. W. H. Sheu, C. H. Yu, and P. H. Chiu, Development of a Dispersively Accurate Conservative Level Set Scheme for Capturing Interface in Two-Phase Flows, *J. Comput. Phys.*, vol. 228, pp. 661–686, 2009.
18. J. von Neumann and R. D. Richtmyer, A Method for the Numerical Calculation on Hydrodynamic Shock, *J. Appl. Phys.*, vol. 21, pp. 232–237, 1950.
19. H. Wang, H. K. Dahle, R. E. Ewing, M. S. Espedal, R. C. Sharpley, and S. Man, An ELLAM Scheme for Advection-Diffusion Equations in Two Dimensions, *SIAM J. Sci. Comput.*, vol. 20, pp. 2160–2194, 1995.
20. P. Tamamidis and D. N. Assanis, Evaluation of Various High-Order-Accuracy Schemes with and without Flux Limiters, *Int. J. Numer. Meth. Fluids*, vol. 16, pp. 931–948, 1993.
21. U. Ghia, K. N. Ghia, and C. T. Shin, High-RE Solutions for Incompressible Flow Using the Navier-Stokes Equations and a Multigrid Method, *J. Comput. Phys.*, vol. 48, pp. 387–411, 1982.
22. D. S. Kumar, K. S. Kumar, and M. K. Das, A Fine Grid Solution for a Lid-Driven Cavity Flow Using Multigrid Method, *Eng. Appl. Comput. Fluid Mech.*, vol. 3, pp. 336–354, 2009.

APPENDIX: COEFFICIENTS OF THE LAGRANGIAN MULTIPLIERS

The derived expressions of the Lagrangian multipliers $\lambda_1 - \lambda_{11}$ in Section 4 are summarized below.

$\lambda_1 = \left(-\frac{8}{27}\pi + \frac{1}{18}\pi^2\right)a_5 - \frac{\pi^2}{36} + \frac{8\pi}{27}$	$\lambda_2 = \left(-\frac{4}{27}\pi + \frac{1}{36}\pi^2\right)a_5 - \frac{\pi^2}{72} + \frac{4\pi}{27}$
$\lambda_3 = \left(\frac{4}{27}\pi - \frac{1}{36}\pi^2\right)a_5 + \frac{\pi^2}{72} - \frac{4\pi}{27}$	$\lambda_4 = \left(\frac{8}{27}\pi - \frac{1}{18}\pi^2\right)a_5 + \frac{\pi^2}{36} - \frac{8\pi}{27}$
$\lambda_5 = 0$	$\lambda_6 = \left(-\frac{4}{27}\pi + \frac{1}{36}\pi^2\right)a_5 - \frac{\pi^2}{72} + \frac{4\pi}{27}$
$\lambda_7 = 0$	$\lambda_8 = 0$
$\lambda_9 = \left(\frac{4}{27}\pi - \frac{1}{36}\pi^2\right)a_5 + \frac{\pi^2}{72} - \frac{4\pi}{27}$	$\lambda_{10} = \left(-\frac{4}{27}\pi + \frac{1}{36}\pi^2\right)a_5 - \frac{\pi^2}{72} + \frac{4\pi}{27}$
$\lambda_{11} = \left(-\frac{8}{27}\pi + \frac{1}{18}\pi^2\right)a_5 - \frac{\pi^2}{36} + \frac{8\pi}{27}$	